Mid-infrared spectroscopy of the Andromeda galaxy

D. Hemachandra[1]⋆, P. Barmby[1], E. Peeters[1,2], S.P. Willner[3], M.L.N. Ashby[3], H.A. Smith[3], K.D. Gordon[4], D.A. Smith[4], and G.G. Fazio[3]

[1] *Department of Physics and Astronomy, University of Western Ontario, London, ON, N6A 3K7, Canada*
[2] *SETI Institute, 189 Bernardo Avenue, Suite 100, Mountain View, CA 94043, USA*
[3] *Harvard-Smithsonian Center for Astrophysics, Cambridge, MA 02138, USA*
[4] *Space Telescope Science Institute, 3700 San Martin Drive, Baltimore, MD 21218, USA*

ABSTRACT

We present *Spitzer*/Infrared Spectrograph 5–21 μm spectroscopic maps towards 12 regions in the Andromeda galaxy (M31). These regions include the nucleus, bulge, an active region in the star-forming ring, and 9 other regions chosen to cover a range of mid-to-far-infrared colours. PAH feature ratios (6.2 μm and 7.7 μm features compared to the 11.3 μm feature) measured from our extracted M31 spectra are consistent with those seen in other nearby galaxies. Our observations did not reproduce the suppressed 6–8 μm features and enhanced 11.3 μm feature seen with the ISOCAM instrument on the Infrared Space Observatory. The equivalent widths of the main PAH features decrease with increasing radiation hardness, consistent with that observed for other nearby spiral and starburst galaxies. The nucleus does not show any PAH emission except for the 11.3 μm feature but does show strong silicate emission at 9.7 μm. Both of these characteristics provide evidence for a low luminosity active galactic nucleus in M31.

Key words: galaxies: individual: M31 – galaxies: ISM – galaxies: nuclei – infrared: ISM – ISM: molecules – ISM: lines and bands

1 INTRODUCTION

Mid-infrared spectra provide a unique diagnostic tool to understand the physical conditions in the interstellar medium of galaxies. The rich range of spectral features (Polycyclic Aromatic Hydrocarbons (PAHs), atomic fine structure lines (e.g. Ne, S) and the amorphous silicate feature centred at 9.7 μm) provide information on dust properties, radiation field and star formation. With the advent of infrared space telescopes, such as the Infrared Space Observatory (ISO, Kessler et al. 1996) and the *Spitzer* Space Telescope (Werner et al. 2004), mid-infrared spectroscopy has become an important method of investigating the infrared emission from galaxies.

PAHs are known as the main carrier of the ubiquitous mid-infrared emission bands (e.g. Allamandola et al. 1989, Puget & Leger 1989). They are large hydrocarbon molecules consisting of ∼50–100 carbon atoms (Tielens 2008). The main PAH features are seen at 3.3, 6.2, 7.7, 8.6, 11.3 and 12.7 μm (e.g., Gillett et al. 1973, Geballe et al. 1985, Peeters 2011), and these bands are due to the vibrational de-excitation of PAH molecules through bending and stretching modes of C-H and C-C bonds (e.g. Allamandola et al.

1989, Puget & Leger 1989). The 6 to 8 micron features are thought to originate mostly from ionized PAHs and the 3.3 and 11.3 μm emission bands from neutral PAHs (e.g. Hudgins & Allamandola 2004 and reference therein, Hony et al. 2001, Galliano et al. 2008a).

The relative strength of the PAH features vary spatially within extended objects and from galaxy-to-galaxy (e.g. Galliano et al. 2008a). While extinction does influence the individual PAH bands to different degrees (e.g. Brandl et al. 2006; Stock et al. 2013), the observed spread in PAH intensity ratios is dominated by the PAH charge balance (Galliano et al. 2008a). In addition, feature ratios do change more drastically close to active galactic nuclei where the overall strength of PAHs also gets weaker (Roche et al. 1991, Smith et al. 2007b). Smith et al. (2007b) found that the mid-infrared spectra from some weak AGNs show suppressed 6 to 8 μm PAH features (by up to a factor of 10 in strength) but are bright at 11.3 μm. One possible explanation for this behaviour is that AGNs alter the grain composition by selective destruction of small ionized PAHs and/or even can excite the PAHs. Alternatively, the PAH emission is modified by the low star formation intensity in the centers of many AGNs (Smith et al. 2007b).

Previous studies of nearby galaxies indicate that metallicity and radiation hardness can both affect the PAH emis-

⋆ E-mail: dhemacha@uwo.ca

sion (e.g. Madden 2000, Beirão et al. 2006, Engelbracht et al. 2008, Muñoz-Mateos et al. 2009). In particular, the PAH equivalent widths (EQWs) in nearby galaxies decrease with increasing radiation hardness, although Brandl et al. (2006) found no such correlation within their starburst sample. In addition, PAH EQWs show an anti-correlation with metallicity in star-forming galaxies. This variation of PAHs among galaxies has also been observed within H II regions of single galaxies (Gordon et al. 2008). But there are no other investigations done on a single star-forming galaxy with sufficiently high resolution to see whether the correlations mentioned above hold within a galaxy similar to the Milky Way.

The amorphous silicate feature at 9.7 μm is another aspect of the mid-infrared spectra of galaxies and in particular their nuclei. Spoon et al. (2007) classified infrared galaxies based on the equivalent width of the 6.2 μm PAH feature and the strength of the 9.7 μm silicate feature. They found galaxies spread along two distinct branches: one in which silicate absorption strength was anti-correlated with PAH equivalent width, and another in which the weak silicate feature strength did not depend on the 6.2 μm equivalent width. Silicate *emission* at 9.7 μm has also been observed in both Seyfert 1 and Seyfert 2 galaxies and can be used to constrain the geometry and structure of the emitting nuclear region (Mason et al. 2009).

M31 with its proximity (785 $\pm$ 25 kpc; McConnachie et al. 2005) and rich observational databases provides the most detailed view of a star forming galaxy similar to the Milky Way. The active star forming ring visible in 8 μm *Spitzer*/IRAC images (Barmby et al. 2006) provides evidence of abundant PAHs in M31. However, ISOCAM spectro-imaging observations of M31(Cesarsky et al. 1998) showed that four regions including the nucleus and bulge of this galaxy have very odd PAH spectra, bright at 11.3 μm while showing weak or no 6.2, 7.7, and 8.6 micron bands. Investigating this unusual PAH emission was the main motivation for the work described in this paper. The centre of M31 has a complicated physical structure. It hosts a very inactive supermassive black hole with a mass of $0.7 - 1.4 \times 10^8$ M$_\odot$ (Bacon et al. 2001; Bender et al. 2005) and also has a lopsided nuclear disk with two stellar components (Lauer et al. 1993) and an A-star cluster (Bender et al. 2005). While M31's nucleus is known to be inactive from an X–ray perspective (Li et al. 2011), mid-infrared indicators of its nuclear activity, such as infrared excess or spectral features of silicates, have received relatively little attention. The higher spatial resolution available in observations of a very nearby galaxy like M31, compared to luminous, distant objects such as ultra-luminous infrared galaxies (Spoon et al. 2007) or nearby Seyferts (Mason et al. 2009), makes exploring its mid-infrared spectrum worthwhile.

We employed mid-infrared spectral maps from the *Spitzer*/Infrared Spectrograph (IRS) from 12 regions of M31 for a further investigation of its infrared properties. This sample includes the nucleus, bulge, an active region in the star-forming ring (all previously observed by ISOCAM), and 9 other regions chosen to cover a range of properties as described in Section 2.1. We obtained the processed version of ISOCAM observations of M31 and compare them with the IRS results in Section 3.1. Section 4.1 discusses PAH intensity ratios. In Section 4.2, we investigate the relationship between PAH equivalent widths and radiation hardness and

Figure 1. $8 - 24/70 - 160$ μm colour-colour diagram of M31 obtained from IRAC and MIPS imaging. Colour-coding of points represents 24 μm flux, from faintest (blue) to brightest (red). The plot is divided into 9 regions (black grid), and the observations were made to cover those regions subject to a 24 μm brightness cut. The black triangles indicate colours of the regions we observed.

compare to that found by Engelbracht et al. (2008) and Gordon et al. (2008). Metallicity and PAH EQWs are compared in Section 4.3, and Section 4.4 discusses the dust properties of the nucleus.

2   OBSERVATIONS AND DATA REDUCTION

2.1   IRS observations

We obtained mid-infrared spectral maps of 12 regions in M31 using the *Spitzer*/IRS instrument (Houck et al. 2004) covering wavelengths from 5 to 21 microns. These regions include the nucleus, the 'bulge' and 'active' regions previously observed by ISOCAM (the latter is Region 9 in our sample), and 9 other regions chosen to cover a range of metallicities and dust temperatures. The 9 regions were chosen by convolving the IRAC 8 μm (Barmby et al. 2006) and MIPS (Gordon et al. 2006) maps to the same resolution and constructing an $8 - 24/70 - 160$ μm colour-colour diagram (Figure 1). This colour space was used to give a rough definition of the types of spectral energy distribution; the dense region in the plot was split into a 3x3 grid and one pixel in each grid region (subject to a a 24μm brightness cut) was selected for spectroscopy. The locations of the observed regions are shown in Figure 2, and their coordinates are given in Table 1. A background observation was also made off the galaxy along the minor axis for use in background subtraction from the data cubes.

For our observations we used the IRS Short-Low (SL) and Long-Low (LL) modules, which cover wavelengths from 5 to 21 microns. The Low modules have resolving power in the range 60–130. Each low-resolution module is divided into two sub-slits which provide spectroscopy in either first or second order. They are denoted as SL1 (7.5–14.5 μm), SL2 (5.2–7.6 μm), LL1 (20.5–38.5 μm, not used in these observations), and LL2 (14.5–20.75 μm). All M31 regions were

Table 1. Spitzer/IRS Target Locations in M31

Name	R.A. (J2000)	Decl. (J2000)	R_{gc}[b]	$12 + \log(O/H)$
Nucleus[a]	$00^h 42^m 44\overset{s}{.}31$	$41°16'09\overset{''}{.}4$	0.0	
Bulge[a]	$00^h 42^m 35\overset{s}{.}00$	$41°21'01\overset{''}{.}0$	4.7	8.90 ± 0.03
Region 1	$00^h 41^m 30\overset{s}{.}41$	$40°43'07\overset{''}{.}8$	12.4	9.20 ± 0.20
Region 2	$00^h 45^m 22\overset{s}{.}85$	$41°38'53\overset{''}{.}1$	13.0	9.07 ± 0.02
Region 3	$00^h 40^m 37\overset{s}{.}37$	$41°01'29\overset{''}{.}4$	12.1	8.85 ± 0.01
Region 4	$00^h 41^m 17\overset{s}{.}86$	$41°07'09\overset{''}{.}8$	8.7	8.89 ± 0.06
Region 5	$00^h 43^m 39\overset{s}{.}57$	$41°19'03\overset{''}{.}1$	7.0	8.93 ± 0.08[c]
Region 6	$00^h 43^m 35\overset{s}{.}72$	$41°23'15\overset{''}{.}0$	4.3	8.73 ± 0.08
Region 7	$00^h 40^m 53\overset{s}{.}98$	$40°58'58\overset{''}{.}9$	8.7	8.40 ± 0.08
Region 8	$00^h 42^m 21\overset{s}{.}60$	$41°07'17\overset{''}{.}4$	3.1	8.94 ± 0.08[c]
Region 9[a]	$00^h 41^m 00\overset{s}{.}00$	$40°36'20\overset{''}{.}3$	13.5	8.86 ± 0.02
NGC 206	$00^h 40^m 20\overset{s}{.}20$	$40°44'54\overset{''}{.}0$	9.8	
Background	$00^h 44^m 41\overset{s}{.}80$	$40°58'56\overset{''}{.}0$	29.5	

[a] Regions with ISOCAM data.
[b] De-projected galactocentric distance in kpc
[c] Metallicities obtained from the radial metallicity profile of M31.
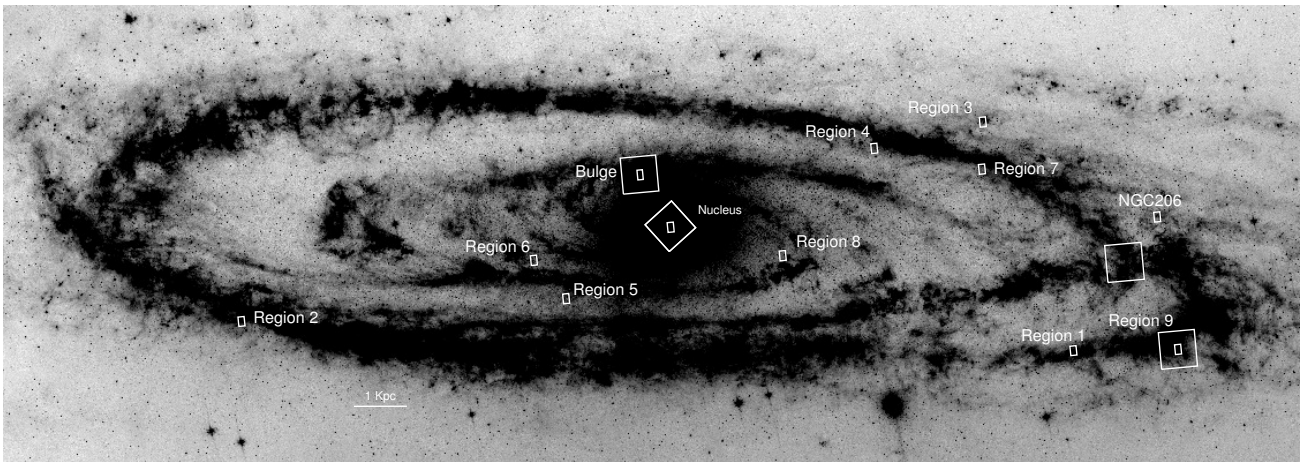
Figure 2. An 8 micron negative IRAC image of M31 (Barmby et al. 2006). Small white rectangles ($30'' \times 50''$) show the regions that we observed, and larger squares ($192'' \times 192''$) show the regions observed by Cesarsky et al. (1998).

observed in September 2007 as part of G. G. Fazio's Guaranteed Time (program ID 40032). The map size was based on the size of the IRS slits (SL: $3.6'' \times 57''$, LL: $10.5'' \times 168''$). Each region was covered by 18 overlapping observations of the SL slit and 11 overlapping observations of the LL slit making the map size $32'' \times 57''$ for SL and $58'' \times 168''$ for LL. Figure 3 shows an example of the slit arrangement. For the brighter regions (nucleus, bulge), ramp times of 14 s (SL) and 30 s (LL) were used, while for the fainter regions, ramp times of 60 and 120 s were used respectively. Background observations were taken with each module (2 per ramp time). Because all of the targets are in the same part of the sky, a common background observation was used for multiple targets to subtract the background emission.

2.2 IRS Data Reduction

The data were reduced through the SSC pipeline (ver. S17.2.0), and the maps were assembled using the CUBISM program (Smith et al. 2007a). Bad pixel removal was also done using CUBISM, and the background observations were

used to subtract the background emission from these cubes following the method outlined by Gordon et al. (2008). Spectra were extracted using a $30'' \times 50''$ rectangular aperture, which corresponds to 114×190 pc at the distance of M31. The aperture size was selected to cover the overlapping area of the SL and LL modes; all the IRS maps cover more area than considered here. In order to study the spatial variation of the emission near the nucleus, we also extracted spectra from two smaller regions within that map.. These will be further discussed in Section 4.4. The spectrum from NGC 206 is very noisy and was removed from our analysis.

There is wavelength overlap between the SL1 and SL2 spectra and also between the SL1 and LL2 spectra. To generate a single spectrum for each M31 region it is necessary to combine the spectra and account for photometric offsets between them. We first combined the extracted SL1 and SL2 spectra by computing the average flux densities over the wavelength overlap region ($7.5 < \lambda < 7.6\mu$m), adding a constant to the SL2 spectra so that they matched the SL1 average, and averaging the SL1 + shifted SL2 spectra over the overlap region. After this procedure there was still a
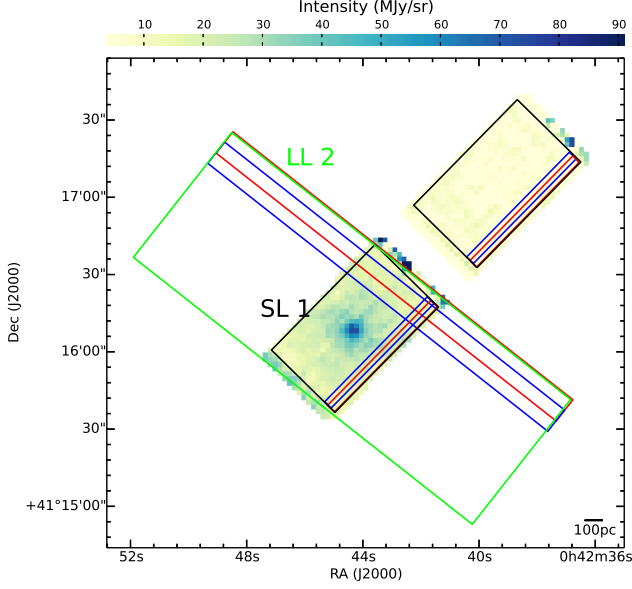
Figure 3. SL1 data cube from the nucleus showing the arrangement of slits used to cover the region. A black box outlines the footprint of the short-low maps and the green box outlines the LL2. Blue and red slits show how each map was covered using overlapping slit positions.

noticeable mis-match between the SL and LL spectra. We addressed this by scaling the SL spectra to match IRAC 8 μm fluxes as follows. IRAC fluxes were measured on the 8 μm image (Barmby et al. 2006) in the same apertures used to extract the IRS spectra and the extended source aperture correction of 0.824 applied. Uncertainties on these measurements were estimated as the standard deviation of the measured IRAC flux in a similarly-sized region off the disk of the galaxy (00$^{\rm h}$48$^{\rm m}$58$^{\rm s}$0, +42°14′54″0). The *Spitzer* synthetic photometry software (Spitzer Science Center 2012) was then used to quantify the colour correction for each spectrum, i.e. the multiplicative factor K between the IRAC photometry over its broad bandpass and the IRS flux density at the centre of the bandpass. The IRAC photometry, IRS flux density, and colour corrections for each region are given in Table 2. Plotting the IRS and colour-corrected IRAC measurements (Figure 4) and fitting a straight line weighted by the uncertainties, we found that the best-fit relation between the measurements had a slope of 0.81 ± 0.08 and intercept of -0.05 ± 0.06. The non-zero intercept of this fit suggested that an additive offset was more appropriate for combining SL and LL spectra than a multiplicative one; this method was also used by Sandstrom et al. (2012). Therefore we scaled each SL spectrum by an offset

$$x = F_{\rm IRAC8}/K - F_{\rm IRS8}. \tag{1}$$

The scaled SL spectra were much better matched to the LL spectra, and the final combination of SL and LL was done using the average-and-offset procedure described above for SL1 and SL2.
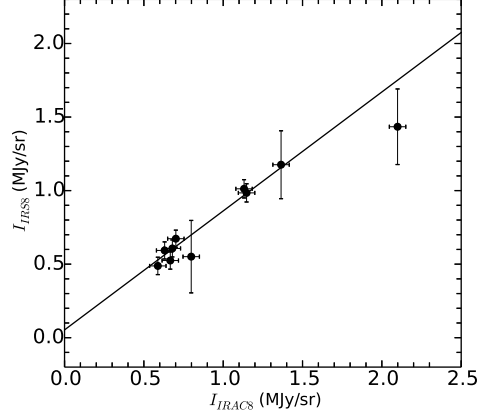
Figure 4. Intensity of the aperture corrected IRAC 8 μm image vs that of the colour corrected IRS spectra at 8 μm obtained using the same aperture for our regions in M31. The straight line is the line of best fit.

Table 2. Matched aperture photometry

Name	IRS[a] MJy sr^{-1}	IRAC[b] MJy sr^{-1}	K[c]	Offset x[d] MJy sr^{-1}
Region 1	1.8505	1.3923	0.532	0.3061
Region 2	1.8238	1.3731	0.555	0.2148
Region 3	0.7192	0.9689	0.767	0.3218
Region 4	1.1431	0.8513	0.589	0.0407
Region 5	0.6787	0.8088	0.773	0.1834
Region 6	0.6399	0.7656	0.927	0.0479
Region 7	1.1538	0.8243	0.526	0.1380
Region 8	0.5556	0.7135	0.877	0.1148
Region 9	1.9413	1.6562	0.606	0.3107
Bulge	2.6956	2.5473	0.532	1.2425

[a]Specific intensity measured at 8.00 μm, no colour correction.
[b]Specific intensity measured over the IRAC 8 μm bandpass, no extended source correction.
[c]Colour correction factor computed from IRS spectrum.
[d]Computed offset between IRAC and IRS as defined in Eq. 1.

2.3 ISOCAM Data Reduction

To compare our results with those of Cesarsky et al. (1998), we retrieved the highly processed ISOCAM data provided by Boulanger et al. (2005) for the nucleus, bulge, and region 9. The ISOCAM data were obtained with the circular variable filters (CVFs) over a $3' \times 3'$ field of view at a scale of $6''$ per pixel. The wavelength range covered was 5.15–16.5 μm at a resolution of $\lambda/\Delta\lambda \approx 45$; the ISOCAM instrument is described by Cesarsky et al. (1996). An image of the ISOCAM data is shown in Figure 5. For the three regions, we extracted spectra using the same $30'' \times 50''$ aperture as for the IRS data.

3 SPECTRAL CHARACTERISTICS AND FEATURE MEASUREMENTS

The final processed IRS spectra are shown in Figure 6, except for the nucleus, discussed in Section 4.4. All of the main
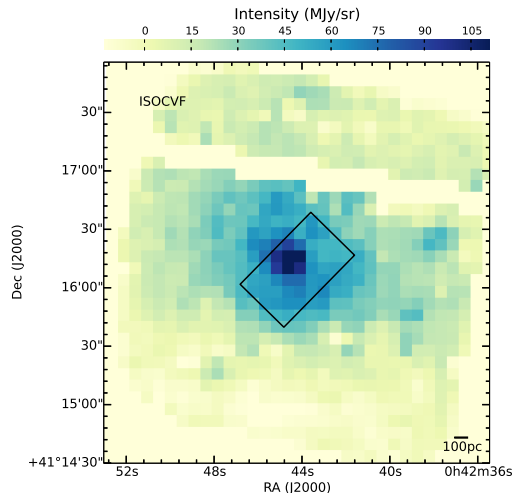
Figure 5. 11.3 μm negative image (dark colours indicate higher flux) of the ISOCAM data cube from the nucleus of M31. The black box shows the size of the aperture ($30'' \times 50''$) used to extract spectra.

PAH features, including the 6.2, 7.7, 8.6 and 11.3 μm bands, are clearly visible for all the regions shown here. The IRS spectra also show atomic line emission such as [Ar II], [Ar III], [S III], [S IV], [Ne II], [Ne III] and molecular H_2 emission at 12.3 μm. Some of the spectra display a contribution to the continuum from starlight emission.

3.1 ISOCAM versus IRS

As mentioned in the Introduction, based on ISOCAM observations of four regions in M31, Cesarsky et al. (1998) reported suppression of the common 6–8 μm PAH bands and a strong 11.3μm PAH band. The 11.3 μm band profile was found to vary from region to region. In addition, Pagani et al. (1999) confirmed that the star-forming ring in M31 shows very weak PAH emission in the 6 to 8 μm region. However, the IRS spectra presented here do not show such unusual behaviour (Figure 6). Indeed, all regions show a normal mid-infrared spectrum similar to other nearby star-forming galaxies.

Until 2005, ISOCAM-CVF data were not properly background subtracted and they were contaminated with zodiacal emission and stray light. Differential spectra between regions of relatively strong and weak emission were previously used to overcome this problem (more details about the differential spectra are given by Cesarsky et al. 1998, Pagani et al. 1999). In 2005, all ISOCAM-CVF data were reprocessed and corrected for the zodiacal emission (Boulanger et al. 2005). We obtained newly-processed ISOCAM spectra from three regions in our IRS sample (see Section 2.3) in order to compare them with the corresponding IRS spectra. Figure 7 shows that although the relative feature intensities in the IRS and ISOCAM spectra differ in detail, the spectral shapes are almost identical; the re-processed ISOCAM data do not agree with the previous differential spectra. Neither the bulge nor Region 9 shows any depletion in 6 to 8 μm features as described by Cesarsky et al. (1998). The new ISOCAM reduction appears to eliminate the discrepancies
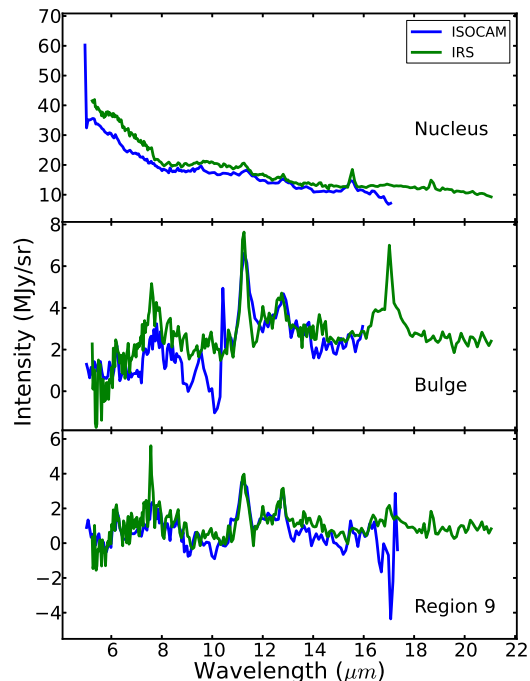
Figure 7. Comparison of IRS and re-processed ISOCAM spectra for the Nucleus (top), Bulge (middle) and Region 9 (bottom) in M31.

between ISOCAM and IRS, resulting in less 'strange' infrared spectra for M31. For the remainder of this work, we discuss only the IRS spectra.

3.2 PAHFIT

The PAH features in the IRS spectra are often blended with neighbouring PAH features and atomic lines. Therefore measuring the strength of PAH features is difficult. To achieve this task a tool called PAHFIT, introduced by Smith et al. (2007b), was used. PAHFIT is an IDL based tool designed for decomposing *Spitzer* IRS low-resolution spectra of PAH emission sources. PAHFIT uses six main components to fit the surface brightness. These are starlight continuum, featureless thermal dust continuum, pure rotational lines of H_2, fine-structure lines, dust emission features and dust extinction. The starlight is represented by blackbody emission at a fixed temperature of 5000 K and the dust continuum is represented by 8 modified blackbodies (emissivity proportional to ν^2) at fixed temperatures of 35, 40, 50, 65, 90, 135, 200, and 300 K. The final fit obtained with PAHFIT does not necessarily use all eight dust components. The infrared extinction is considered as a combination of a power law plus silicate absorption features with peaks at 9.7 and 18 μm. Line features are represented by Gaussian profiles with widths set by the instrumental resolution and dust features are represented by Drude profiles; more details about PAHFIT are given by Smith et al. (2007b).

Initial attempts at fitting the spectra with PAHFIT showed that some components were negligible, and to avoid over-fitting we re-ran the fits without these components.
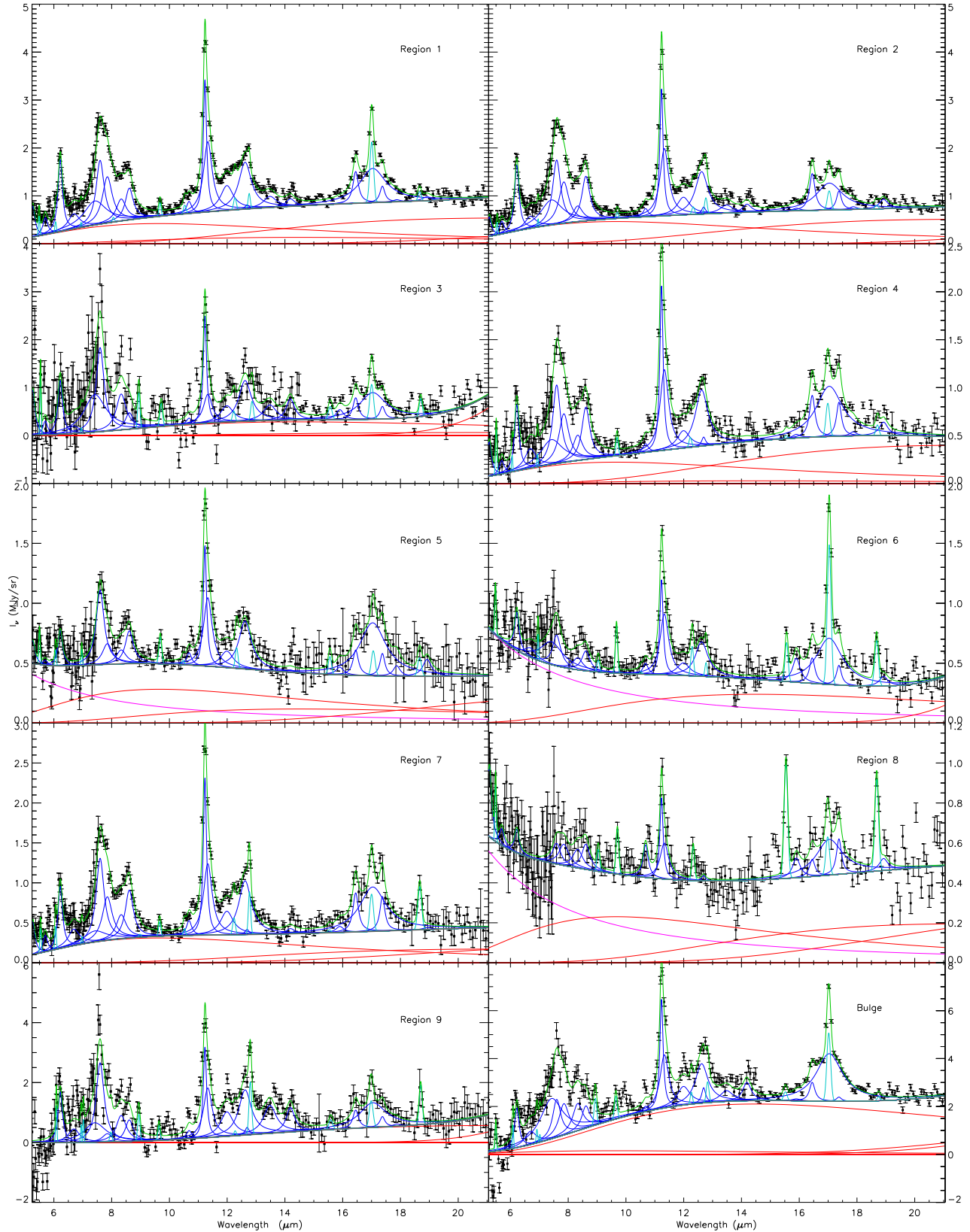
Figure 6. Observed IRS spectra and detailed PAHFIT decompositions (see Section 3.2). Regions are labeled in each panel. Black squares show the observed data, and red, blue, light blue, pink and green lines represent the modelled dust continua, PAH features, atomic lines, starlight continuum and the fit respectively. The black line shows the total modelled continuum. Vertical scales differ in different panels. Spectra from the nucleus and NGC 206 are not shown here.

None of the IRS spectra shows significant silicate absorption around 9.7 or 18 μm and the extinction calculated by PAHFIT was almost zero for all the initial fits. Except for four regions (the bulge, Region 5, Region 6 and Region 8), the starlight contribution is also negligible. We adjusted the PAHFIT input parameters to fix extinction to zero for all regions and starlight to zero for all but the four regions above. Typically only two or three thermal dust components had significant power in our fits, but we did not fix the unused components to zero. Regions 3 and 9 were found to have very low dust continuum emission compared to other spectra, possibly because of noisy data at short wavelengths. However the other features in these spectra appear to be fit correctly. The spectrum of the nucleus shows silicate emission (see Section 4.4), which is not included in PAHFIT; consequently PAHFIT was unable to sucessfully fit the other spectral features in this spectrum.

3.3 PAH features

PAHFIT returns fluxes and equivalent widths (EQWs) of PAH features which are given in Tables 3 and 4. The intensities of the features do not include any contribution from the continuum but the equivalent width computed by

$$\text{EQW} = \int \frac{I_{\nu,\text{feature}}}{I_{\nu,\text{cont}}} \, d\lambda, \tag{2}$$

is a measure of both the strength of the continuum emission ($I_{\nu,\text{cont}}$) and the line strength ($I_{\nu,\text{feature}} = I_\nu = -I_{\nu,\text{cont}}$). The continuum emission is mainly coming from dust grains, much larger than PAH molecules. Hence, by studying EQWs of PAHs, we can study how the PAHs compete with the dust grains in the mid-infrared wavelengths. PAHFIT returns the EQWs for each PAH feature and the uncertainties were calculated using a Monte-Carlo method. In that method, for each region, PAHFIT was run 500 times on randomly generated data points normally distributed within the uncertainties of the spectrum. PAHFIT returned 500 EQWs for each PAH feature and the standard deviation of EQWs for a given feature was taken as its uncertainty. The EQWs from Regions 3 and 9 were removed from further analysis because the negligible dust continuum for these spectra makes the EQWs highly uncertain.

3.4 Atomic line features

PAHFIT also returns the line strengths and uncertainties for atomic lines, listed in Table 5. Not all lines were detected by PAHFIT, so we calculated upper limits for non-detected lines[1] Line ratios of [Ne III]/[Ne II] and [S IV]/[S III] 18 have been used as an indication of the radiation hardness, and Engelbracht et al. (2008) defined a combination of these two line ratios as a 'radiation hardness index (RHI)':

$$\text{RHI} = \left(\log \frac{[\text{Ne III}]}{[\text{Ne II}]} + \left[0.71 + 1.58 \log \frac{[\text{S IV}]}{[\text{S IV}]} \right] \right) / 2 \tag{3}$$

---

[1] To find the upper limits for the flux of missing atomic lines, we assumed the line to be a Gaussian profile with a FWHM as given by PAHFIT. The peak intensity was taken to be 3 times the RMS, where RMS is the root mean square of the noise at the position of a missing line.
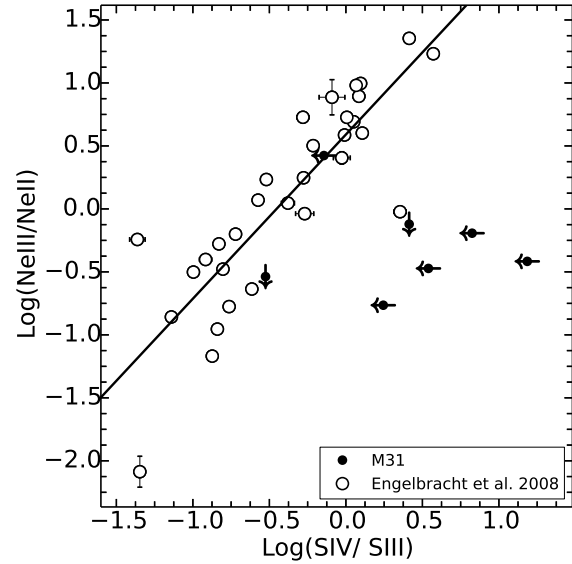
Figure 8. Log([Ne III]/[Ne II]) vs Log([S IV]/[S III]) 18 for the M31 regions in our sample (black dots) and for the starburst sample from Engelbracht et al. (2008) (open dots). The straight line is the line of best fit for the starburst sample.

Here, 1.58 and 0.71 are the slope and the intercept of the [Ne III]/[Ne II] vs [S IV]/[S III] 18 plot (Figure 8) for the starburst sample from Engelbracht et al. (2008). The RHI has also been used by Gordon et al. (2008) for M101 observations. Figure 8 compares the atomic line emission from the selected regions of M31 to the starburst galaxy sample; although none of our spectra have detections of all four lines, our limits are consistent with the trend. We therefore compute the RHI using the first term of equation 3.4 for the regions with missing S lines and the second term for the regions with missing Ne lines. Regions 2, 5, and 8 had detections of only one line per element, so we used the appropriate upper limits to calculate RHI for these spectra.

## 4 RESULTS AND DISCUSSION

4.1 PAH intensities

Both the 6.2 and 7.7 μm features are thought to be coming from ionized PAHs and the 11.3 μm feature from neutral PAHs. Therefore we expect to see a correlation between the intensities of 6.2 and 7.7 μm PAH features normalized by the 11.3 μm feature. In Figure 9 we compare the PAH flux ratios of 7.7/11.3 and 6.2/11.3 features. The figure shows a good correlation between these two PAH line ratios, consistent with that of the SINGS sample shown by Smith et al. (2007b). A similar correlation was also reported by Galliano et al. (2008b) for a sample of galaxies and a handful of extended HII regions and by Vermeij et al. (2002) for Galactic and Magellanic Cloud IIregions. This provides evidence that the PAH emission from M31 is not unusual.

Table 3. PAH Emission Line Strengths[a]

| Region	5.7μm	6.2μm	7.7μm	8.3μm	8.6μm	10.7μm	11.3μm	12.0μm	12.7μm	17.0μm
Region 1	10 ± 1	34 ± 1	107 ± 10	13 ± 1	14.1 ± 0.9	2.2 ± 0.3	33.4 ± 0.9	9.1 ± 0.5	16 ± 1	17 ± 1
Region 2	7.7 ± 0.9	31.2 ± 0.8	106 ± 8	9 ± 1	19.8 ± 0.8	1.5 ± 0.2	32.0 ± 0.8	6.6 ± 0.4	15 ± 1	14.7 ± 0.9
Region 3	8 ± 4	25 ± 3	111 ± 22	21 ± 4	7 ± 3	1.1 ± 0.9	19 ± 3	6 ± 1	14 ± 3	13 ± 2
Region 4	4 ± 1	15.8 ± 0.9	59 ± 9	7 ± 1	11.6 ± 0.8	0.8 ± 0.2	19.9 ± 0.8	3.5 ± 0.4	9 ± 1	12.5 ± 0.9
Region 5	1 ± 1	7 ± 1	22 ± 3	3 ± 1	5.8 ± 0.8	0.9 ± 0.2	12.7 ± 0.8	2.4 ± 0.4	6.3 ± 0.4	10 ± 2
Region 6	- - - -	7.3 ± 0.9	22 ± 7	3 ± 1	3.6 ± 0.8	0.8 ± 0.2	10.8 ± 0.8	1.9 ± 0.4	4.5 ± 0.4	8.3 ± 0.6
Region 7	5.9 ± 0.9	17.7 ± 0.9	57 ± 8	9 ± 1	12.8 ± 0.8	1.6 ± 0.2	21.8 ± 0.8	5.2 ± 0.4	11 ± 1	13 ± 2
Region 8	$2. \pm 1$	3 ± 1	6 ± 3	3 ± 1	2.7 ± 0.8	1.4 ± 0.3	4.4 ± 0.8	- - - -	- - - -	4.1 ± 0.7
Region 9	- - - -	38 ± 3	133 ± 29	25 ± 4	15 ± 3	2.4 ± 0.8	37 ± 3	14 ± 1	25 ± 3	19 ± 6
Bulge	- - - -	38 ± 2	219 ± 27	32 ± 4	20 ± 3	2.0 ± 0.9	53 ± 3	14 ± 1	29 ± 3	39 ± 2

[a]Units are 10^{-9} W m^{-2}.

Table 4. PAH Emission Line Equivalent Widths[a]

Name	5.7μm	6.2μm	7.7μm	8.3μm	8.6μm	10.7μm	11.3μm	12.0μm	12.7μm	17.0μm
Region 1	0.39 ± 0.08	1.2 ± 0.1	3.4 ± 0.3	0.43 ± 0.04	0.47 ± 0.04	0.09 ± 0.01	1.45 ± 0.04	0.43 ± 0.03	0.78 ± 0.03	1.27 ± 0.05
Region 2	0.28 ± 0.04	1.02 ± 0.06	3.4 ± 0.2	0.32 ± 0.04	0.70 ± 0.04	0.07 ± 0.01	1.58 ± 0.04	0.35 ± 0.02	0.85 ± 0.03	1.35 ± 0.06
Region 3[b]	4 ± 2	8 ± 2	19 ± 4	2.8 ± 0.8	0.9 ± 0.5	0.1 ± 0.1	2.1 ± 0.3	0.7 ± 0.2	1.6 ± 0.2	2.4 ± 0.3
Region 4	0.28 ± 0.09	1.0 ± 0.1	3.7 ± 0.4	0.5 ± 0.1	0.77 ± 0.07	0.07 ± 0.02	1.67 ± 0.06	0.31 ± 0.04	0.86 ± 0.05	1.68 ± 0.07
Region 5	- - - -	0.12 ± 0.03	0.61 ± 0.08	0.10 ± 0.03	0.20 ± 0.03	0.05 ± 0.01	0.77 ± 0.03	0.17 ± 0.03	0.50 ± 0.04	1.6 ± 0.2
Region 6	- - - -	0.10 ± 0.04	0.6 ± 0.2	0.10 ± 0.04	0.14 ± 0.03	0.05 ± 0.01	0.77 ± 0.04	0.15 ± 0.03	0.42 ± 0.04	1.7 ± 0.1
Region 7	0.32 ± 0.05	0.86 ± 0.06	2.8 ± 0.2	0.44 ± 0.06	0.69 ± 0.06	0.12 ± 0.02	1.81 ± 0.07	0.48 ± 0.05	1.11 ± 0.08	2.2 ± 0.2
Region 8	0.03 ± 0.04	0.04 ± 0.03	0.2 ± 0.10	0.09 ± 0.04	0.10 ± 0.03	0.09 ± 0.02	0.30 ± 0.02	0.00 ± 0.00	0.01 ± 0.01	0.62 ± 0.07
Region 9[b]	- - - -	237 ± 100	151 ± 60	16 ± 6	8 ± 3	0.5 ± 0.2	7 ± 1	2.3 ± 0.6	3.6 ± 0.8	2.4 ± 0.8
Bulge	- - - -	1.2 ± 0.2	4.0 ± 0.4	0.51 ± 0.07	0.30 ± 0.06	0.03 ± 0.01	0.78 ± 0.03	0.22 ± 0.02	0.49 ± 0.03	1.16 ± 0.04

[a]Units are μm. [b]Continuum for these regions is very weak. Equivalent widths are highly uncertain and not considered in the analysis (see Section 3).
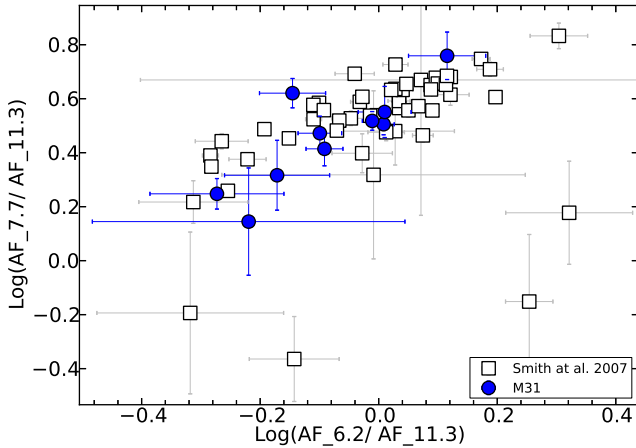
Figure 9. Ratios of PAH feature fluxes (7.7 μm/11.3 μm versus 6.2 μm/11.3 μm) for 10 regions in M31. Open squares represent the SINGs sample from Smith et al. (2007b).

4.2 PAH equivalent widths versus radiation hardness

As mentioned in the introduction, PAH equivalent widths tend to show an inverse correlation with radiation hardness. The equivalent widths of the M31 PAH features are compared with RHI in Figures 10 and 11. For reference, we also show the starburst sample of Engelbracht et al. (2008),
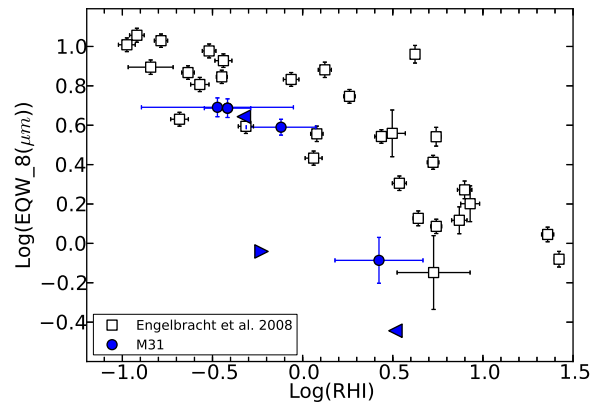
Figure 10. Equivalent width of the 8 μm PAH feature versus radiation hardness index (RHI) for the M31 sample (blue). The 8μm feature is a combination of the 7.7, 8.3 and 8.6 μm PAHFIT components. Open squares represent the starburst galaxy sample from Engelbracht et al. (2008). For M31 spectra with undetected lines, triangles represent upper (left-pointing triangles) and lower (right-pointing triangles) limits.

which includes 66 nearby $(2 < d < 250$ Mpc) star-bursting or star-forming galaxies selected to cover a wide range in metallicity $(7.1 < 12 + \log[\mathrm{O/H}] < 8.9)$, and the seven H II regions in M101 observed by Gordon et al. (2008), which have $8.1 < 12 + \log[\mathrm{O/H}] < 8.8$. To make a direct compari-

Table 5. Atomic Emission Line Strengths[a]

Name	[Ar II] 7.0μm	[Ar III] 9.0μm	[S IV] 10.5μm	[Ne II] 12.8μm	[Ne III] 15.5μm	[S III] 18.7μm
Region 1	<15.2	<16.4	6 ± 1	6 ± 1	< 4.2	2.2 ± 0.4
Region 2	5 ± 3	< 17.4	<5.1	6 ± 1	< 2.9	0.9 ± 0.5
Region 3	<42.9	27 ± 6	< 28.9	9 ± 3	6 ± 1	4.3 ± 0.9
Region 4	<11.2	<10.0	<4.4	2 ± 1	0.6 ± 0.5	1.3 ± 0.5
Region 5	4 ± 3	<6.2	< 5.2	< 4.2	2 ± 1	2 ± 1
Region 6	7 ± 3	4 ± 2	< 3.8	2 ± 1	5.4 ± 0.5	5.3 ± 0.5
Region 7	3 ± 3	<12.6	2.3 ± 0.9	10 ± 2	< 2.9	8 ± 1
Region 8	<11.8	5 ± 2	<4.9	<2.6	11.6 ± 0.5	6.5 ± 0.5
Region 9	24 ± 10	35 ± 8	< 2.7	38 ± 3	7 ± 4	15.3 ± 5.6
Bulge	10 ± 7	49 ± 7	< 30.4	19 ± 4	7 ± 2	2 ± 1

[a]Units are 10^{-10} W m^{-2}. Upper limits are indicated with a < mark.
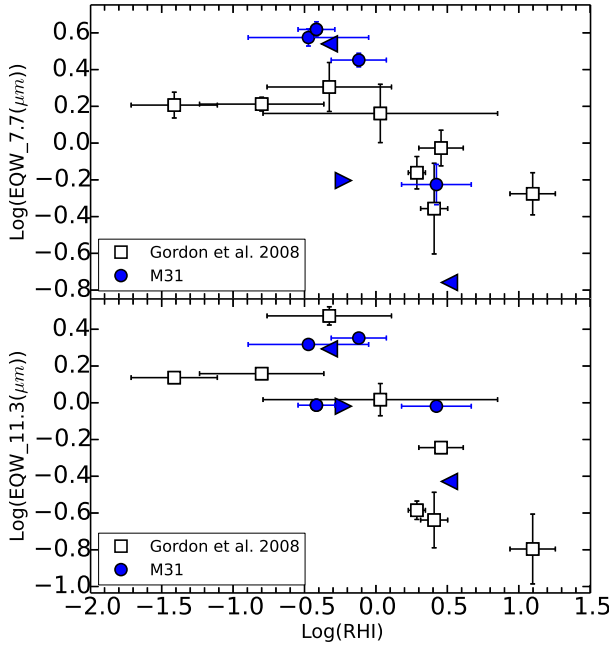
Figure 11. Equivalent widths of the normalized 7.7 μm PAH feature (top panel) and 11.3 μm PAH feature (bottom panel) versus radiation hardness index (RHI) for the M31 sample. Open squares represent the data from M101 by Gordon et al. (2008). The normalization was done by dividing each EQW by the weighted average over all regions in the respective samples. Triangles represent upper and lower limits.

son with the M101 sample, we normalized the M31 EQWs in Figure 11 using the same procedure as Gordon et al. (2008), dividing each EQW by the weighted average over all regions in the respective samples. The equivalent widths seem to be decreasing with increasing radiation hardness, consistent with previous results. This also helps to confirm that the PAH emission in M31 is not unusual.

4.3 PAH equivalent widths versus metallicity

Many studies based on ISO and *Spitzer* observations have reported that PAH intensity decreases with decreasing metallicity (Calzetti et al. 2010). In addition, these studies also

report a sudden drop of EQWs of PAHs around 12 + log (O/H) ≈ 8.1. This has been observed amongst different galaxies (Engelbracht et al. 2008) as well as within a single galaxy (Gordon et al. 2008).

Here we investigate the relation between the PAH features and the metallicity for the M31 regions in this paper. As a source of metallicity measurements, we used the work of Sanders et al. (2012) who measured spectroscopic metallicities for more than 250 H II regions using strong line diagnostics.[2] Except for regions 5 and 8, all of our mapped regions contain an H II region measured by Sanders et al. (2012), and we give the corresponding metallicities in Table 1. For regions 5 and 8 we adopted metallicities from the radial metallicity profile of M31 given by Sanders et al. (2012). It is well known that there are systematic differences between different methods used to measure metallicities, and those in the sample of Engelbracht et al. (2008) were obtained by the direct electron temperature method (Skillman et al. 1998). Croley et al. (2014) calculated the offset between direct and strong-line measurements for M31 H II regions to be 0.35 ± 0.10. In Figure 12 we have corrected for this offset by subtracting 0.35 from our metallicities.

Figure 12 shows the normalized EQWs of the PAH features versus the metallicity for our sample and the starburst galaxies of Engelbracht et al. (2008). The scatter in our sample is large, but the equivalent widths of the 7.7 and 11.3 μm features are not inconsistent with those of Engelbracht et al. (2008). However, we do not have enough data from low-metallicity regions in M31 to observe the expected decrease of EQWs of PAH with the decreasing metallicity. There do seem to be some outliers which can plausibly be due to the uncertainties and the offset between different methods of calculating the metallicity.

4.4 Dust properties of the nucleus

The extracted IRS spectrum of the M31 nuclear region (Figure 13) looks different from most of the other spectra, with a blue continuum, PAH features weak or absent at 6–8 μm but

[2] Sanders et al. (2012) considered several different calibrations for abundance diagnostics. We use the results from the method they denote "N06 N2" (Nagao et al. 2006) because that method has the largest sample size.
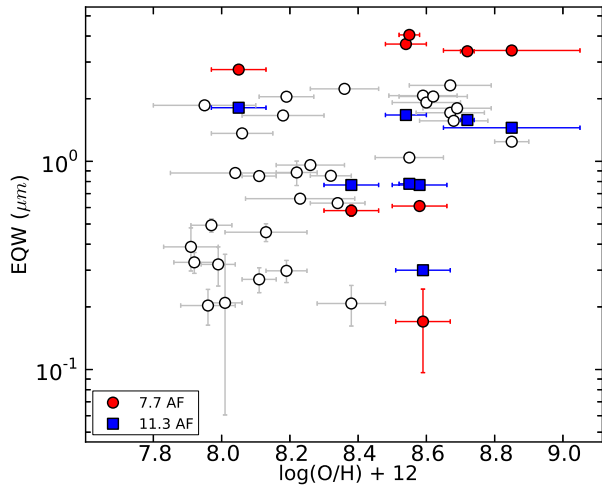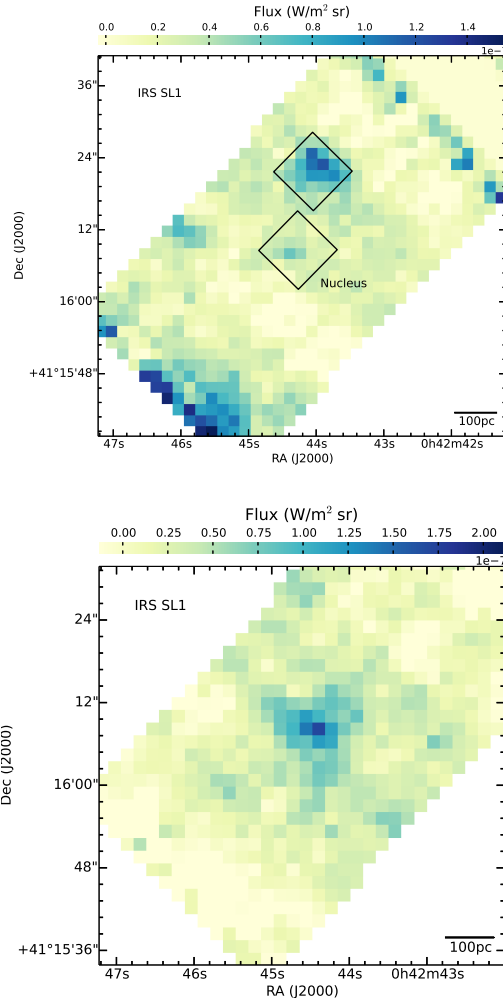
Figure 12. PAH equivalent widths versus metallicity. EQWs of the 7.7 μm feature of the starburst sample from Engelbracht et al. (2008) are plotted in open circles.

Figure 13. Here is where we show the PAHFIT analysis of the nucleus spectrum.

detectable at 11.3 μm. **NEED some further discussion of the nuclear spectrum in general here.** Figure 14 (top) shows the integrated intensity map of 11.3 μm emission around the nucleus. The majority of the 11.3 μm emission is from a region north of the nucleus and not from the nucleus itself. On the other hand the centre shows no PAH emission, but it does have silicate emission around 9.7 μm, which comes only from the nucleus and is not present in the North spectrum (see Figure 14 (bottom), a continuum-subtracted image which shows the 9–11 μm integrated emission). Both the 11.3 μm and silicate emission sources are consistent with being unresolved point sources. We extracted spectra from the centre and the North region using a $9'' \times 9''$ square aperture as shown in Figure 14.

The mid-infrared spectra of the nucleus from both *Spitzer* and ISOCAM (Figure 7) show similar characteristics: a blue continuum, PAH features weak or absent at 6–8 μm but detectable at 11.3 μm, and detectable atomic fine structure lines. Comparing the M31 nuclear spectrum with the nuclear spectra from the SINGS sample given by Smith et al. (2007b), we found six other galaxies with similar spectral shapes, including three elliptical galaxies, two spirals, and a lenticular.[3] The SINGS papers (Kennicutt et al. 2003; Smith et al. 2007b; Moustakas et al. 2010) are in some disagreement over the exact nuclear spectral types of these six galaxies. All are classified as some form of low-luminosity AGN such as Seyfert or LINER (luminous AGNs were intentionally omitted from the SINGS sample Kennicutt et al. 2003), but they are by no means the only LLAGN in the SINGS sample. In contrast with the nuclear spectrum, the
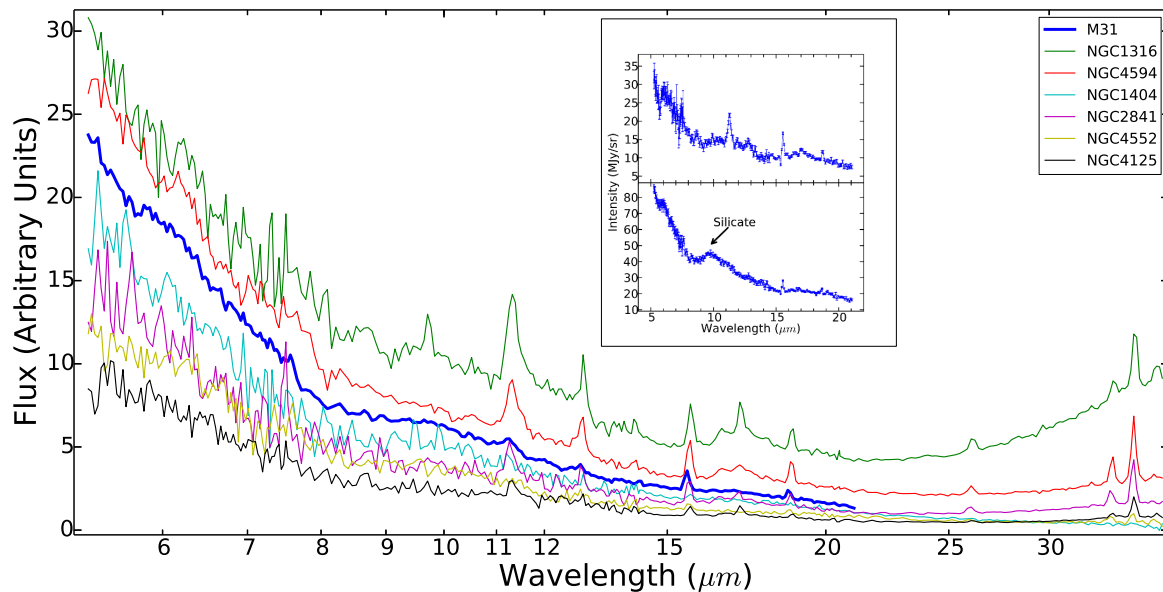
[3] The IRS spectra for the SINGS galaxies were extracted over areas ranging from 2 to 8 kpc^2, whereas the M31 nucleus spectrum covers a much smaller area (0.02 kpc^2).

Figure 14. (Top): Intensity variation of 11.3 μm emission around the nucleus of M31. Two black boxes are the apertures (centre and north region) used to extract spectra in Figure 15. The centre of the nucleus is at R.A. $00^{\rm h}42^{\rm m}44{\rm s}35$, Dec. $+41°16'08''5$ (Garcia et al. 2010). (Bottom:) Integrated strength of the silicate emission (from 9 to 11 μm) near the M31 nucleus.

spectrum extracted in the North region (offset by $''$ from the center; Figure 15, inset) shows a strong 11.3 μm peak and no significant emission from 6–8 μm features. These characteristics are shared by the M81 nuclear spectrum presented by Smith et al. (2010), although that spectrum has little stellar continuum and a very strong [Ne II] 12.8 μm line.

As discussed by Smith et al. (2007b) and Smith et al. (2010), inferring the suppression of 6–8 μm PAH features compared to the 11.3 μm feature must be done with caution, since the 6–8 μm features are more susceptible to dilution by the stellar continuum. Such suppression could have several causes: destruction of small or charged PAH molecules by an AGN, or weak ultraviolet continuum indicating lack of star formation (Smith et al. 2007b). In the latter case, the AGN is not the cause of the suppressed 6–8 μm features, but rather is only detected when the nuclear star formation rate is low. An implication of low star formation in the centre of M31 is consistent with previous work: although Melchior & Combes (2013) found a significant amount of cold gas in the centre

Figure 15. Mid-infrared spectrum of the nucleus of M31 (blue) over-plotted with spectra extracted close to the nuclei of 6 nearby galaxies which have AGN activity (Smith et al. 2007b). NGC 4552, NGC 1404 and NGC 4125 are elliptical galaxies and NGC 4594 and NGC 2841 are spiral galaxies. NGC 1316 is a lenticular galaxy. The inset shows the spectra extracted from the centre region of the M31 nucleus (bottom) and from the north region (top) shown in Figure 14.

of the galaxy, this gas does not appear to be associated with current star formation. In modelling the far-infrared spectral energy distribution, Groves et al. (2012) found that the old stellar population in the M31 bulge is sufficient to heat the observed dust; no young stellar population is needed.

Examining the spatial distribution of the mid-infrared emission in the M31 nuclear region provides additional clues to the nature of the emitting sources. Figure 14 shows that most of the 11.3 μm comes from a region to the north of the nucleus, while the silicate emission (Figure 14, bottom) is centred on the nucleus itself. Figure 15 compares the spectra extracted from these two regions. Silicate emission is not very common in integrated spectra of galaxies (Spoon et al. 2007) but is seen in luminous quasar spectra (Hill et al. 2014) and, as mentioned above, in the spectrum of the M81 nucleus. We computed the linear slope parameter defined by Smith et al. (2010), $\gamma 810 = [F_\nu(10\mu m) - F_\nu(8\mu m)]/2F_\nu(9\mu m)$, for the M31 nucleus and found $\gamma 810 = -0.08 \pm 0.06$. This is

Does detection of silicate emission in the M31 nuclear spectrum imply the detection of an active nucleus? In the unified model of AGNs, an obscuring torus viewed face-on would be expected to show silicate emission (Efstathiou & Rowan-Robinson 1995; Spinoglio & Malkan 1992); however such a view would also be expected to show forbidden atomic lines such as [Ne v] and [S iv], not seen in the M31 spectrum. Alternatively, Mason et al. (2012) explained that low-luminosity AGNs cannot host a Seyfert-like obscuring torus because of their optically thin dust and low dust-to-gas ratio, but can show the silicate emission that originates in the optically thin hot dust around the torus. The first detection of such silicate emission was reported by Sturm et al. (2005) from the low-ionization nuclear emission-line region (LINER) galaxy NGC 3998, and Mason et al. 2012 observed that this 9.7 μm silicate emission is present in many

LLAGNs. We computed the bolometric luminosity of the M31 nucleus to be (**value goes here**) erg s^{-1} using the 12 μm flux and the method described in Spinoglio & Malkan (1989). This value is close to that of other LLAGNs (**and consistent with the X–ray value?**)

5 SUMMARY AND CONCLUSIONS

We obtained *Spitzer*/IRS spectral maps of 12 regions within M31 covering wavelengths 5–21 μm. The spectra from those regions, except for the nucleus, are similar to spectra obtained from other nearby star-forming galaxies. However, our spectra are inconsistent with previous ISOCAM observations of M31 (Cesarsky et al. 1998) which reported a suppression of the 6–8 μm features and an enhancement of 11.3 μm feature towards 4 regions. Our IRS spectra for three of these regions do not show this unusual behaviour and neither do spectra extracted from the reprocessed version of the ISOCAM data. We conclude that the earlier results based on ISOCAM data were likely affected by the background subtraction methods applied.

The PAH intensities in M31 regions showed a decreasing trend with increasing radiation hardness, consistent with previous results from other nearby galaxies. The distribution of PAH EQWs with metallicity was well within the range of the starburst galaxy sample of Engelbracht et al. (2008). We did not have enough data from low-metallicity regions of M31 to observe the decreasing trend of EQWs at low metallicities which is visible in other galaxies.

Mid-infrared spectra from near the nucleus of M31 show either suppressed 6–8 μm features and a strong 11.3 μm feature (off-nucleus, GIVE DISTANCE) or silicate emission around 9.7 μm (on-nucleus). The off-nucleus region spectrum is similar to that of six other nearby galaxies

known to have low-luminosity AGN activity. This could strengthen the suggestion by Smith et al. (2007b) that low $L(7.7\mu m)/L(11.3\mu m)$ is an indicator of low luminosity AGN, but this feature ratio could also be due to a lack of ionized PAHs. The nuclear silicate emission is another possible AGN indicator and should be further explored.

REFERENCES

Allamandola L. J., Tielens A. G. G. M., Barker J. R., 1989, ApJS, 71, 733
Bacon R., Emsellem E., Combes F., Copin Y., Monnet G., Martin P., 2001, A&A, 371, 409
Barmby P., et al., 2006, ApJ, 650, L45
Beirão P., Brandl B. R., Devost D., Smith J. D., Hao L., Houck J. R., 2006, ApJ, 643, L1
Bender R., et al., 2005, ApJ, 631, 280
Boulanger F., et al., 2005, A&A, 436, 1151
Brandl B. R., et al., 2006, ApJ, 653, 1129
Calzetti D., et al., 2010, Conference Proceedings 'Reionization to Exoplanets', ed. P. Ogle, ASP Conference Series,
Cesarsky C. J., et al., 1996, A&A, 315, L32
Cesarsky D., Lequeux J., Pagani L., Ryter C., Loinard L., Sauvage M., 1998, A&A, 337, L35
Croley M., Barmby P., Stock D., Azimlu M., Rosolowsky E., 2014, MNRAS, submitted
Efstathiou A., Rowan-Robinson M., 1995, MNRAS, 273, 649
Engelbracht C. W., Rieke G. H., Gordon K. D., Smith J.-D. T., Werner M. W., Moustakas J., Willmer C. N. A., Vanzi L., 2008, ApJ, 678, 804
Galliano F., Madden S., Tielens A., Peeters E., Jones A., 2008a, ApJ, 679, 310
Galliano F., Madden S. C., Tielens A. G. G. M., Peeters E., Jones A. P., 2008b, ApJ, 679, 310
Garcia M. R., et al., 2010, ApJ, 710, 755
Geballe T. R., Lacy J. H., Persson S. E., McGregor P. J., Soifer B. T., 1985, ApJ, 292, 500
Gillett F. C., Forrest W. J., Merrill K. M., 1973, ApJ, 183, 87
Gordon K. D., et al., 2006, ApJ, 638, L87
Gordon K. D., Engelbracht C. W., Rieke G. H., Misselt K. A., Smith J.-D. T., Kennicutt Jr. R. C., 2008, ApJ, 682, 336
Groves B., et al., 2012, MNRAS, 426, 892
Hill A. R., Gallagher S. C., Deo R. P., Peeters E., Richards G. T., 2014, MNRAS, 438, 2317
Hony S., Van Kerckhoven C., Peeters E., Tielens A. G. G. M., Hudgins D. M., Allamandola L. J., 2001, A&A, 370, 1030
Houck J. R., et al., 2004, ApJS, 154, 18
Hudgins D. M., Allamandola L. J., 2004, in Witt A. N., Clayton G. C., Draine B. T., eds, Astronomical Society of the Pacific Conference Series Vol. 309, Astrophysics of Dust. p. 665
Kennicutt Jr. R. C., et al., 2003, PASP, 115, 928
Kessler M. F., et al., 1996, A&A, 315, L27
Lauer T. R., et al., 1993, AJ, 106, 1436
Li Z., Garcia M. R., Forman W. R., Jones C., Kraft R. P., Lal D. V., Murray S. S., Wang Q. D., 2011, ApJ, 728, L10
Madden S. C., 2000, New A Rev., 44, 249
Mason R. E., Levenson N. A., Shi Y., Packham C., Gorjian V., Cleary K., Rhee J., Werner M., 2009, ApJ, 693, L136
Mason R. E., et al., 2012, AJ, 144, 11
McConnachie A. W., Irwin M. J., Ferguson A. M. N., Ibata R. A., Lewis G. F., Tanvir N., 2005, MNRAS, 356, 979
Melchior A.-L., Combes F., 2013, A&A, 549, A27
Moustakas J., Kennicutt Jr. R. C., Tremonti C. A., Dale D. A., Smith J.-D. T., Calzetti D., 2010, ApJS, 190, 233
Muñoz-Mateos J. C., et al., 2009, ApJ, 703, 1569
Nagao T., Maiolino R., Marconi A., 2006, A&A, 459, 85
Pagani L., Lequeux J., Cesarsky D., Milliard B., Lionard L., Sauvage M., 1999, A&A, 351, 447
Peeters E., 2011, in IAU Symposium. pp 149–161, arXiv:1111.3680, doi:10.1017/S174392131102494X
Puget J. L., Leger A., 1989, ARA&A, 27, 161
Roche P. F., Aitken D. K., Smith C. H., Ward M. J., 1991, MNRAS, 248, 606
Sanders N. E., Caldwell N., McDowell J., Harding P., 2012, ApJ, 758, 133
Sandstrom K. M., et al., 2012, ApJ, 744, 20
Skillman E. D., Terlevich E., Terlevich R., 1998, Space Sci. Rev., 84, 105
Smith J.-D. T., et al., 2007a, PASP, 119, 1133
Smith J.-D. T., et al., 2007b, ApJ, 656, 770
Smith H. A., et al., 2010, ApJ, 716, 490
Spinoglio L., Malkan M. A., 1989, ApJ, 342, 83
Spinoglio L., Malkan M. A., 1992, ApJ, 399, 504
Spitzer Science Center 2012, Spitzer Data Analysis Cookbook, v5.0.1 edn. SSC, Pasadena, CA
Spoon H. W. W., Marshall J. A., Houck J. R., Elitzur M., Hao L., Armus L., Brandl B. R., Charmandaris V., 2007, ApJ, 654, L49
Stock D. J., Peeters E., Tielens A. G. G. M., Otaguro J. N., Bik A., 2013, ApJ, 771, 72
Sturm E., et al., 2005, ApJ, 629, L21
Tielens A. G. G. M., 2008, ARA&A, 46, 289
Vermeij R., Peeters E., Tielens A. G. G. M., van der Hulst J. M., 2002, A&A, 382, 1042
Werner M. W., et al., 2004, ApJS, 154, 1

This paper has been typeset from a TeX/ LaTeX file prepared by the author.